Title:

Why SARS-CoV-2 Omicron variant is milder? A single high-frequency mutation of structural envelope protein matters.

Author:

Bingqing Xia[1,2,*], Yi wang[1,3], Xiaoyan pan[4], Xi Cheng[1,2], Hongying Ji[1], Xiaoli Zuo[1],Jia Li[1,2], Zhaobing Gao[1,2,*]

[1] CAS Key Laboratory of Receptor Research, Stake Key Laboratory of Drug Research, Shanghai Institute of Materia Medica, Chinese Academy of Sciences, 555 Zuchongzhi Road, Shanghai, 201203, China.

[2] University of Chinese Academy of Sciences, 19A Yuquan Road, Beijing, 100049, China.

[3] State Key Laboratory of Medical Neurobiology, Institutes of Brain Science, Fudan University, Shanghai 200032, China.

[4] State Key Laboratory of Virology, Wuhan Institute of Virology, Center for Biosafety Mega-Science, Chinese Academy of Sciences, Wuhan, 430071, China.

These authors contributed equally: Bingqing Xia, Yi wang

*Corresponding author. Email: zbgao@simm.ac.cn (Z.G.), xiabingqing@simm.ac.cn (B.X.).

Abstract:

SARS-CoV-2 Omicron variant is highly transmissible and extensive morbidity, which has raised concerns for antiviral therapy. In addition, the molecular basis for the attenuated pathogenicity and replication capacity of Omicron remains elusive. Here, we report for the first time that a high-frequency mutation T9I on 2-E of SARS-CoV-2 variant Omicron forms a non-selective ion channel with abolished calcium permeability and reduced acid sensitivity compared to the WT channel. In addition, T9I caused less cell death and a weaker cytokine production. The channel property changes might be responsible for the Omicron variant releases less efficiently and induces a comparatively lower level of cell damage in the infected cells. Our study gives valuable insights into key features of the Omicron variant, further supporting 2-E is a promising drug target against SARS-CoV-2 and providing critical information for the COVID-19 treatment.

35 **Main Text:**

36 Since November 2021, a new SARS-CoV-2 variant (B.1.1.529) emerged in South
37 Africa and was designated as the fifth variant of concern (VOC), named as Omicron [1,
38 2]. Omicron variant is highly transmissible and extensive morbidity, which has raised
39 concerns for antiviral therapy. Omicron has largest number (>30) of substitutions,
40 deletions, or insertions with mutations frequency higher than 1% in the spike protein
41 (S). Mutation studies in the spike RBD domain have provided a plausible explanation
42 for altered transmissibility and antibody resistance [3-5]. Recent reports revealed Omicron
43 variant induces a longer cycle for virus shed, attenuates replication capacity, and
44 produces substantially attenuated lung pathology, indicating that the pathogenic ability
45 of Omicron variant is indeed milder [6-8]. However, the molecular basis for the attenuated
46 pathogenicity and replication capacity remains elusive. The envelope protein of SARS-
47 CoV-2 (2-E) forms a homo-pentameric cation channel that is important for virus
48 pathogenicity[9, 10]. It has been demonstrated that 2-E channel alone is sufficient to induce
49 cell death, provoke cytokine storm and even cause acute respiratory distress syndrome
50 (ARDS)-like damages *in vivo*. Its inhibitor exhibits excellent antiviral activity *in vivo*[9].
51 Therefore, we focus on the 2-E mutations of Omicron variant.

52 Three high quality E protein sequences of Omicron variants (B.1.1.529, BA1, BA2) in
53 the CNCB database as of January 18 th, 2022 (https://ngdc.cncb.ac.cn/ncov/) were
54 comprehensively analyzed and a mutation T9I caught our attention. Compared with the
55 original Wuhan reference strain, among more than one hundred identified 2-E

mutations in Omicron variant, T9I shows a much higher frequency than the rest mutations. In addition, the mutation probability of T9I in all statistical samples is higher than 99.5%. In particular, for the most common Omicron strain B.1.1.529, the mutation probability is 100% (Fig.1a, b). According to the solved NMR structure, T9 locates at the top of the transmembrane domain (TMD) of E protein [10]. The influence of T9I has not been studied yet completely.

First, we asked whether 2-E^{T9I} (T9I) still retains its channel activity. We purified the T9I protein and reconstituted the protein on Planar Lipid Bilayer (BLM) (Supplementary Fig.S1). The observed T9I-induced typical single-channel currents supports that T9I was able to form ion channels also as wild-type proteins. However, the reversal potential of T9I channels was shifted to the left, from 57 mV to 3 mV, under asymmetric KCl solutions. Similar reversal potential shifting was also detected in asymmetric NaCl solutions (Fig.1c.d, Supplementary Fig.S2). A reversal potential close to 0 mV suggests that T9I may have lost its selectivity to cations. To determine whether T9I can permeate chloride，the channel activity of T9I was further examined in asymmetric 50:500 mM choline chloride solutions. Choline chloride is a quaternary ammonium salt containing choline cation and chloride anion, which is always to detect anion permeability. As expected, outward currents were indeed observed when the holding voltage potentials were higher than the theoretical reversal potential for chloride (E_{rev}> 70 mV). 2-E^{WT} (WT) channels are permeable to Ca^{2+}. As shown in Figure S2c, for WT channels, the frequent and continuous inward potassium currents in the asymmetric 50:500 mM (trans: cis) K^+ solutions indicated that the 2-E channels

were incorporated into the membranes. The membrane potential was then changed to +65 mV (K^+ reverse potential) to eliminate the K^+ currents. Intriguingly, outward step-like signals appeared when 20 mM (final concentration) Ca^{2+} was added to the *trans* side. When the Ca^{2+} concentration increased to 20 mM, the outward currents increased. In contrast, under the identical conditions, T9I channels did not induce detectable calcium currents (Supplementary Fig.S2c). These results revealed that T9I owns a different ion selectivity and permeability from WT. WT channels are pH sensitive [9]. The pH influences on T9I channels were evaluated on a same channel using titration strategy. After the channels incorporated into the membranes, HCl was titrated into either *cis* or *trans* side to alter the pH to 4 from 6. Consistent to our previous results, reduction of pH, either in *cis* or *trans* side, induced significant increase of channel amplitude and open probability. In contrast, pH reduction in cis side failed to increase the channel activity of T9I. Although we didn't have direct evidences to explain how the threonine (T9) site is sensitive to pH changes, the structure of 2-E channels supported the residues around T9 were sensitive to pH change including Glu7 and Glu8 side chain carboxyl could be deprotonated at neutral pH and protonated at acidic pH [10]. It is reported that SARS-CoV-2 traffics to the lysosomes for egress by lysosome deacidification, instead of using the conventional biosynthetic secretory pathway [11]. The E channel of coronavirus is localized to intracellular organelles, including lysosome and Golgi apparatus [11, 12]. The cellular localization and expression of WT and T9I were assessed by immunocytochemistry and confocal microscopy. We found that both WT and T9I are co-localized with the lysosomal marker LAMP (Fig.1g,

100 supplementary Fig.S3). Given the localization on lysosome, the influences of WT and
101 T9I on the luminal pH of lysosome were compared. We used flow cytometric analysis
102 of a ratio metric pHluorin molecule. This pH probe consists of green fluorescent protein
103 (GFP) pHluorin molecule fused with lysosome-resident protein CD63. To generate a
104 pH calibration curve, un-transfected cells were subjected to treatment with buffers
105 ranging from pH 5.5 to 7.5 in the presence of the ionophores monensin and nigericin
106 prior to flow analysis (Fig.1h, i). Expression of WT channels robustly neutralized the
107 lysosome pH, whereas T9I channels exhibited less influences in luminal pH, which was
108 consistent with our electrophysiological results (Fig.1j). Therefore, the capability of
109 deacidification of 2-E channels in lysosomes was significantly impeded by the mutation
110 T9I. Based on above, whether the weakened capability of deacidification hampers virus
111 releasing was examined. We transfected the Vero E6 cells with WT or T9I plasmids at
112 day 1, then the cells were infected with SARS-CoV-2 virus at day 2. As determined by
113 qRT-PCR, pre-expression of mutant T9I significantly attenuated viral loadings
114 compared with WT (Fig.1k). It was logic to deduce that some exogenous ^{T9I} subunits
115 would co-assemble with the wild type subunits from the virus and form
116 heteromultimers with impaired pH sensitivity, resulting in less deacidification of
117 lysosomes and less SARS-CoV-2 virus releasing.

118 Finally, the channel activity of the 2-E protein is a determinant of virulence. We used
119 Annexin V/PI staining and CCK8 assays to evaluate the cell lethality of T9I in Vero E6
120 cells. We found that heterogeneously expression of T9I caused similar cell death with
121 WT (Fig. 1 l, Fig.1g, supplementary Fig.S4a). In the mouse macrophage cell line

122 (RAW264.7), T9I induced a similar increase of inflammatory cytokines with WT also
123 (Fig. 1m, Supplementary Fig.S4b). However, in the case of comparable cell lethality
124 and cytokine releasing level, the expression level of T9I was far exceeding the
125 expression level of WT (Fig. 1 n). The correlation between the cell lethality and the
126 expression level was further compared. As shown in Figure 1o, the killing cells
127 capability of T9I was dropped around 150 times as well as the cytokines production.
128 Notably, the 2-E expression in Omicron variant was decreased approximately 3-fold,
129 which may further suppress the virulence of Omicron variants [6]. Consistently, it has
130 been demonstrated that the ability of Omicron to induce cell death was indeed abolished
131 within 48 hours [6]. How much the weakened virulence of T9I confers the milder clinical
132 symptoms of Omicron warrants further investigation.

133 Overall, as SARS-CoV-2 infections are progressing, there are chances that virus
134 accumulates new mutations. Among existed antiviral targets, different from spike
135 protein, RNA-dependent RNA polymerase (Rdrp) and 3CL pro, which mediate virus
136 entry, protein cleavage and viral replication, the envelope protein (2-E) majorly
137 participating in the virus releasing [13-15]. Here we report for the first time that a high-
138 frequency mutation T9I on 2-E of SARS-CoV-2 variant Omicron forms a non-selective
139 ion channel with abolished calcium permeability and reduced acid sensitivity compared
140 to the WT channel. In addition, T9I caused less cell death and a weaker cytokine
141 production (Fig.1p). The channel property changes might be responsible for the
142 Omicron variant releases less efficiently and induces a comparatively lower level of
143 cell damage in the infected cells. According to 2-E NMR structures, although T9I is not

located in the pore domain of the channel, it may alter the channel configuration via interacting with the amino acids at positions L12 and T11lining the pore (Supplementary Fig.S5). Our study gives valuable insights into key features of the Omicron variant, further supporting 2-E is a promising drug target against SARS-CoV-2 and providing critical information for the COVID-19 treatment.

Acknowledgement:

We are grateful to the National Science Fund of Distinguished Young Scholars (81825021), Fund of Youth Innovation Promotion Association (2019285), the National Natural Science Foundation of China (81773707, 31700732), the National Key Research and Development Program of China (2020YFC0842000), the Strategic Leading Science and Technology Projects of Chinese Academy of Sciences (XDA12050308), Fund of National Science and Technology Major Project (2018ZX09711002-002-006) and the Hubei Science and Technology Project (2020FCA003) for financial support.

Author contributions:

Z. G., and B. X. conceived designed the project. Z. G., J. L., and B. X designed the experiments; Y. W. and B. X. performed the electrophysiological recordings; B. X. carried out the cell-based assays; P. X. carried out the virus assays in vitro; Y. W purified the proteins; H.Y. analyzed the sequence; all authors analyzed and discussed the data. Z. G., B. X. wrote the manuscript. All authors read and approved the manuscript.

Reference:

165 1 Karim SSA, Karim QA. Omicron SARS-CoV-2 variant: a new chapter in the COVID-
166 19 pandemic. *Lancet (London, England)* 2021; **398**:2126-2128.
167 2 Organization WH. Classification of Omicron (B.1.1.529): SARS-CoV-2 Variant of
168 Concern. <https://wwwwhoint/news/item/26-11-2021-classification-of-omicron-
169 (b11529)-sars-cov-2-variant-of-concern>.
170 3 Cao Y, Wang J, Jian F *et al.* Omicron escapes the majority of existing SARS-CoV-2
171 neutralizing antibodies. *Nature* 2021.
172 4 Cele S, Jackson L, Khoury DS *et al.* Omicron extensively but incompletely escapes
173 Pfizer BNT162b2 neutralization. *Nature* 2021.
174 5 Bojkova D, Widera M, Ciesek S, Wass MN, Michaelis M, Cinatl J, Jr. Reduced
175 interferon antagonism but similar drug sensitivity in Omicron variant compared to
176 Delta variant of SARS-CoV-2 isolates. *Cell research* 2022:1-3.
177 6 Shuai H, Chan JF, Hu B *et al.* Attenuated replication and pathogenicity of SARS-
178 CoV-2 B.1.1.529 Omicron. *Nature* 2022.
179 7 Halfmann PJ, Iida S, Iwatsuki-Horimoto K *et al.* SARS-CoV-2 Omicron virus causes
180 attenuated disease in mice and hamsters. *Nature* 2022.
181 8 Torjesen I. Covid-19: Peak of viral shedding is later with omicron variant, Japanese
182 data suggest. *BMJ (Clinical research ed)* 2022; **376**:o89.
183 9 Xia B, Shen X, He Y *et al.* SARS-CoV-2 envelope protein causes acute respiratory
184 distress syndrome (ARDS)-like pathological damages and constitutes an antiviral target.
185 *Cell research* 2021; **31**:847-860.
186 10 Mandala VS, McKay MJ, Shcherbakov AA, Dregni AJ, Kolocouris A, Hong M.

Structure and drug binding of the SARS-CoV-2 envelope protein transmembrane domain in lipid bilayers. *Nature structural & molecular biology* 2020; **27**:1202-1208.

11 Ghosh S, Dellibovi-Ragheb TA, Kerviel A *et al.* β-Coronaviruses Use Lysosomes for Egress Instead of the Biosynthetic Secretory Pathway. *Cell* 2020; **183**:1520-1535.e1514.

12 Westerbeck JW, Machamer CE. The Infectious Bronchitis Coronavirus Envelope Protein Alters Golgi pH To Protect the Spike Protein and Promote the Release of Infectious Virus. *Journal of virology* 2019; **93**.

13 Yin W, Mao C, Luan X *et al.* Structural basis for inhibition of the RNA-dependent RNA polymerase from SARS-CoV-2 by remdesivir. *Science (New York, NY)* 2020; **368**:1499-1504.

14 Jin Z, Du X, Xu Y *et al.* Structure of M(pro) from SARS-CoV-2 and discovery of its inhibitors. *Nature* 2020; **582**:289-293.

15 Liu L, Wang P, Nair MS *et al.* Potent neutralizing antibodies against multiple epitopes on SARS-CoV-2 spike. *Nature* 2020; **584**:450-456.

Figure:

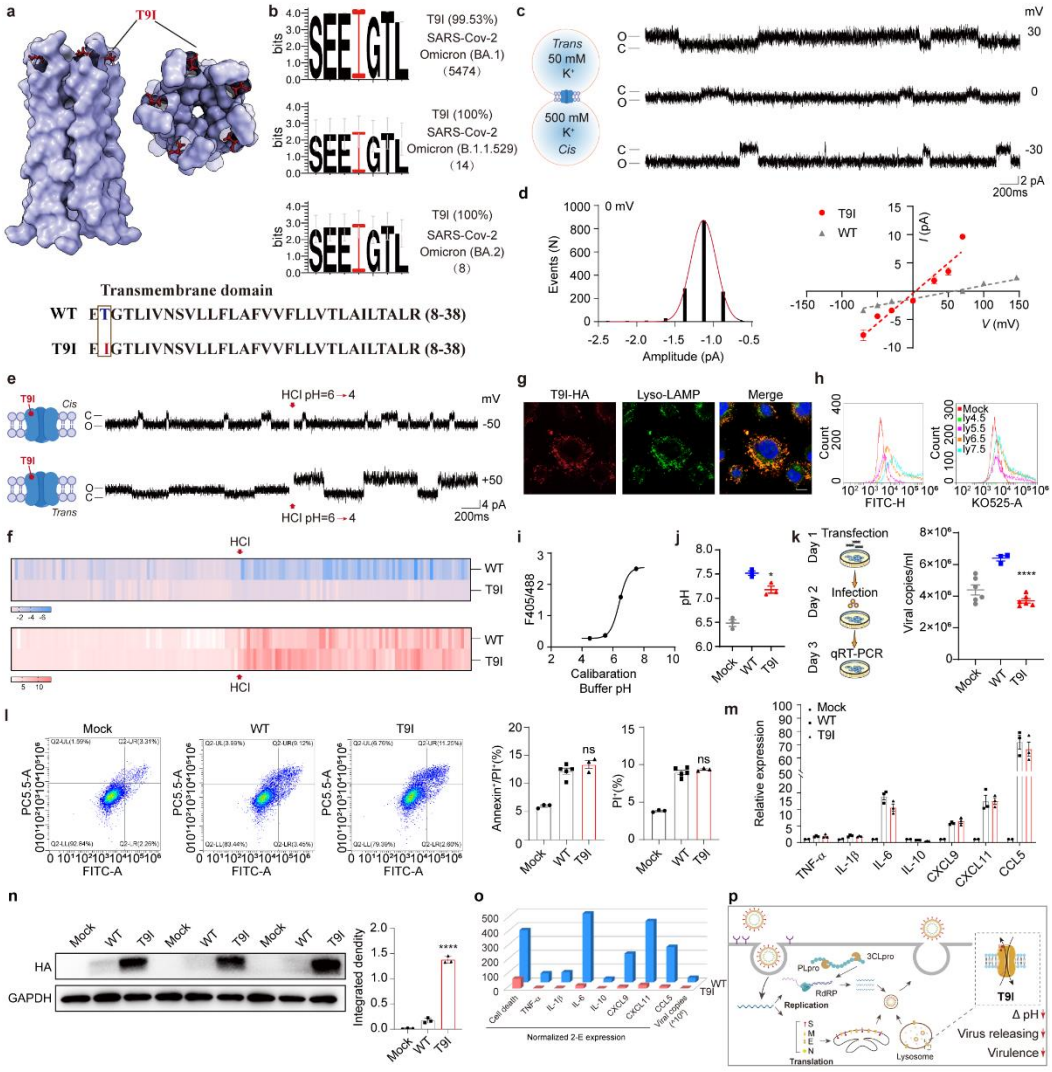

Fig.1 The envelope protein mutation T9I of SARS-CoV-2 Omicron variant shows less pathogenicity and weakens virus production.

a, Structure of the 2-E TM domain [10]. Illustration of the amino-acid sequence of SARS-CoV-2 E (8-38) and the indicated mutants. Threonine residues (T) are marked as blue and the T >I mutants are marked as red. **b,** 2-E protein amino-acid sequence logo of SARS-CoV-2 Omicron variant. The I9 residues are marked as red. 2-E protein sequences were downloaded from China National Center for Bioinformation (CNCB) using the "Lineage Browse" option. Logos were generated using the WebLogo 3.7.4

212 online tool. **c,** Single-channel current recording of T9I after reconstitution in lipid
213 bilayers with PC/PS = 3:2 lipids at indicated potentials and solutions (Left). **d,** Left, all-
214 point current histograms for the trace in **c** (0 mV) ("C" means Closed; "O" means Open).
215 Right, *I-V* curves of T9I in the solutions of **c** ($n \geq 3$). **e**, Single-channel current recording
216 in 500 :500 mM KCl solutions via proton titration result in different pH (*cis* or *trans*).
217 Red arrow represents titration of HCl. **f,** The heat map shows the transition of the
218 currents from panel **e** under proton titration. **g,** Cell immunofluorescence of T9I (Red)
219 and lysosome marker LAMP (Green). T9I is co-localized with lysosome. **h-j,** Lyso-pH
220 indicator was used to assess the pH of the lysosome via flow cytometry. Flow cytometry
221 pattern of the cells in buffers of known pH and contained ionophores to equilibrate the
222 extracellular and lysosome luminal pH (**h**). Calibration curves were generated from data
223 like those illustrated in h (**i**). **j,** The pH value of Vero E6 cells lysosome transfected with
224 WT, T9I or Mock. **k.** Flow chart of the experiment (Left), the virus copies in supernatant
225 determined by qRT-PCR assay (Right). MOI of SARS-CoV-2 for infection was 0.01. **l,**
226 Flow cytometry pattern of Vero E6 cells transfected with WT or T9I plasmids. Right,
227 flow cytometry analysis of Propidium iodide (PI) and Annexin V stained Vero E6 cells.
228 **m,** Serum cytokine levels at 24 h after transfection with WT, T9I or Mock detected by
229 RT-qPCR. **n,** Protein expression levels of WT and T9I in Vero E6 cells after transfection
230 (Left). The histogram shows the quantization of the result (Right). **o,** The relative
231 activity of WT, T9I in pH regulation, cell virulence, channel conductance and viral
232 copies normalized to the expression levels. **p,** Life cycle pattern diagram of SARS-
233 CoV-2 Omicron variant. T9I on envelope protein (2-E) of SARS-CoV-2 variant

Omicron forms a non-selective ion channel with weakened pathogenicity and virus production. Experiments were independently performed thrice and similar results were obtained. One set of reprehensive data is shown here ($n \geqslant 3$). $^{*}p < 0.05$; $^{**}p < 0.01$; $^{***}p < 0.001$; unpaired Student's t test. All error bars are SEM.

239 **Method:**

240 **Plasmids and mutagenesis**

241 Wild type SARS-CoV-2-E sequences were synthesized by the Beijing Genomics
242 Institute (BGI, China). The mutants 2-E^{T9I} sequence was generated by site-directed
243 mutagenesis and confirmed by sequencing (BGI, China). Vector pET28a was used for
244 protein purification; vector pcDNA5 and pcDNA3.1 were used for cell survival assay
245 and cell imaging.

246 **Cell culture and treatment**

247 Vero E6 and Raw 264.7 cells were grown in 90% DMEM basal medium (Gibco, USA)
248 supplemented with 10% fetal bovine serum (Gibco, USA) at 37°C under 5% CO_2.

249 **Planar lipid bilayers recording**

250 According to our previous methods, the purified protein 2-E^{WT} or 2-E^{T9I} were
251 incorporated into lipid bilayers to test their functionality. The lipid bilayers were
252 prepared by PC: PS= 3: 2 (Avanti Polar Lipids, USA). Proteins were added in *cis* side
253 and the solution was 50:500 mM (*trans*: *cis*) KCl or others, all solutions were buffered
254 by 5mM HEPES, pH 6.35. Membrane currents were recorded by headstage connected
255 with amplifier BC-535 (Warner Instruments, USA), filtered at 1–2 kHz and digitized
256 by Axon Digidata 1440A (Molecular Devices, USA). The recording frequency was 10
257 kHz. The data were processed using pClamp 10.2 software (Molecular Devices, US).
258 The single-channel conductance was determined by fitting to Gaussian functions (bin

259 width = 0.25 pA). Opening time less than 0.5–1.5 ms was ignored to avoid noise
260 interference. The equilibrium potential was calculated using Goldman–Hodgkin–Katz
261 flux equation:

262 $$E_m = \frac{RT}{F} \ln \left(\frac{P_{Na^+}[Na^+]_{out} + P_{Cl^-}[Cl^-]_{in} + P_{K^+}[K^+]_{out}}{P_{Na^+}[Na^+]_{in} + P_{Cl^-}[Cl^-]_{out} + P_{K^+}[K^+]_{in}}\right)$$

263

264 **Cell viability and cytotoxicity assay**

265 Cell viability was measured by the CCK-8 kit (40203ES60, Yeason, China) according
266 to the manufacturer's instructions. The absorbance was measure at 450 nm with Thermo
267 Scientific Microplate Reader (Thermo Fisher Scientific Inc., USA).

268 **Western blotting and antibodies**

269 Proteins were resolved in 12% SDS-PAGE, transferred to PVDF membranes (GE,
270 USA). The PVDF membranes were incubated with primary antibodies against HA-Tag
271 (C29F4) (3724, CST, USA) or GAPDH (30201ES20, Yeasen, China), then incubated
272 with second antibodies against IgG (Yeasen, China).

273 **Flow cytometry of cell death**

274 After treatment, cells were detached, collected by centrifugation and resuspended in 1×
275 binding buffer containing 100 μg/mL propidium iodide (PI) and Annexin V-FITC (1:20,
276 V13242, Life, USA) and incubated at room temperature for 15 min in the dark.
277 Subsequently, samples were added 400 μL of 1× binding buffer and kept on ice. Cells
278 were analyzed by flow cytometry using BD FACSCALIBUR 4 (BD COMPANY, USA).

279 The percentages of differently labeled cells were calculated by FlowJo 7.6.

280 **Immunofluorescence microscopy.**

281 Vero E6 cells were seeded as 1×10^4 cells per well in coverslips on chamber slides
282 (Thermo Fisher Scientific Inc., USA) overnight. Cells were transfected with WT or T9I
283 with lysosome marker (LAMP1,). After transfection for 24 h, cells were washed with
284 phosphate-buffered saline (PBS) and fixed in 4% paraformaldehyde for 10 min at room
285 temperature. Then the cells were permeabilized in 0.5% Triton X-100 in PBS for 3
286 min. The coverslips were washed twice with PBS and incubated with primary antibody
287 in 1% bovine serum albumin (BSA) (36101ES25, Yeasen, China) for 2 h at room
288 temperature. Anti-HA (HT301-01, Trans, China) and rabbit anti-LAMP (55273-1-AP,
289 Proteintech, USA) were used to incubate the cells at a 1:1,000 dilution. Then, second
290 antibodies FITC-AffiniPure Goat Anti-Rabbit IgG (33107ES60, Yeasen, China) and
291 Cy3-AffiniPure Goat Anti-Mouse IgG (33208ES60, Yeasen, China)were used to
292 incubate the cells at a 1:1,000 dilution. Images were captured using the Leica TCS-SP8
293 STED system with 100× oil objective.

294 **Virus loading and quantitative real-time PCR (qRT-PCR) analysis**

295 SARS-CoV-2 (nCoV-2019BetaCoV/Wuhan/WIV04/2019) was preserved at Wuhan
296 institute of virology, Chinese Academy of Sciences. It was propagated and titrated with
297 Vero E6 cells, and its associated operations were performed in a biosafety level 3 (BSL-
298 3) facility. Cell supernatants RNA was isolated with MiniBEST Viral RNA/DNA
299 Extraction Kit (Takara, Japan) as described in the instruction, and cDNA was

300 transcribed with PrimeScript^{TM} RT reagent Kit with gDNA Eraser (Takara, Japan). In
301 detail, 50 μL supernatant were collected for RNA isolation with a MiniBEST Viral
302 RNA/DNA Extraction Kit Ver.5.0 (Takara, AK41820A), and the total RNA was eluted
303 with 30 μL RNase-free water. cDNA was transcribed from 3 μL total RNA in 20 μL
304 reaction system with PrimeScriptTM RT reagent Kit with gDNA Eraser (Takara,
305 AK71648A). Viral copies were quantified from 1 μL template viral cDNA by a standard
306 curve method on ABI 7500 (Takara TB Green Premix Ex Taq II, AK81975A) with a
307 pair of primers targeting S gene. The forward primer (5'-3') is:
308 CAATGGTTTAACAGGCACAGG; the reverse primer (5'-3') is:
309 CTCAAGTGTCTGTGGATCACG.

310 **Determination of lysosome pH**

311 Vero cells were transfected with Lyso-pHluorin (addgene,70113) and 2-E plasmid.
312 After transfection, cells were trypsinzed and washed with Live Cell Imaging Solution
313 (LCIS). Then, replaced LCIS with cellular pH calibration Buffers containing 10 μM
314 Valinomycin and Nigericin (Intracellular pH Calibration Buffer Kit, P35379, Themo,
315 USA) and incubate at 37°C for at least 5 minutes. At last, cells were analyzed via Flow
316 cytometry with excited at 405 nm and 488 nm, and the emission signals were collected
317 with detection filters at 500 to 550 nm and 515 to 545 nm, respectively. Flow cytometric
318 data were collected and quantified using CytoExpert 2.4 software.

319 **Homology modeling**

320 The solid-state NMR structure of SARS-CoV-2 envelope protein (PDB code: 7k3g)

321 [(2020) Nat Struct Mol Biol 27: 1202-1208] was used to as the template to build
322 homology models of the mutant envelope protein. This solid-state data yield to ten
323 lowest-energy structures. These ten structures were employed to construct ten
324 homology models of the mutant envelope protein using Modeller [A. Sali, T.L. Blundell,
325 Comparative protein modelling by satisfaction of spatial restraints, J Mol Biol 234
326 (1993) 779-815. 10.1006/jmbi.1993.1626.]. The models with the lowest root mean
327 square deviations from their template structures were selected.

328 **Statistics**

329 All measurements were derived from distinct samples. Statistics were performed in
330 GraphPad Prism. Statistical significance was determined by one-way ANOVA and two-
331 way ANOVA followed by pairwise Student's t-test with Tukey's or Sidak's correction.
332 Two-tailed unpaired Student's t test was performed if only two conditions were
333 compared. Data in the text is presented as Mean ± SEM. Adjusted P values are reported
334 in the figures.
335

Supplementary figure：

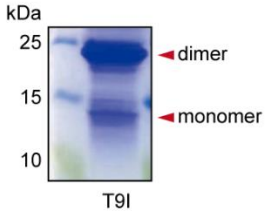

Supplementary information, Fig. S1 Purification of T9I proteins. Purification of full-length 2-E^{T9I} protein with Ni-NTA affinity chromatography. 15% SDS-PAGE gel with coomassie blue staining.

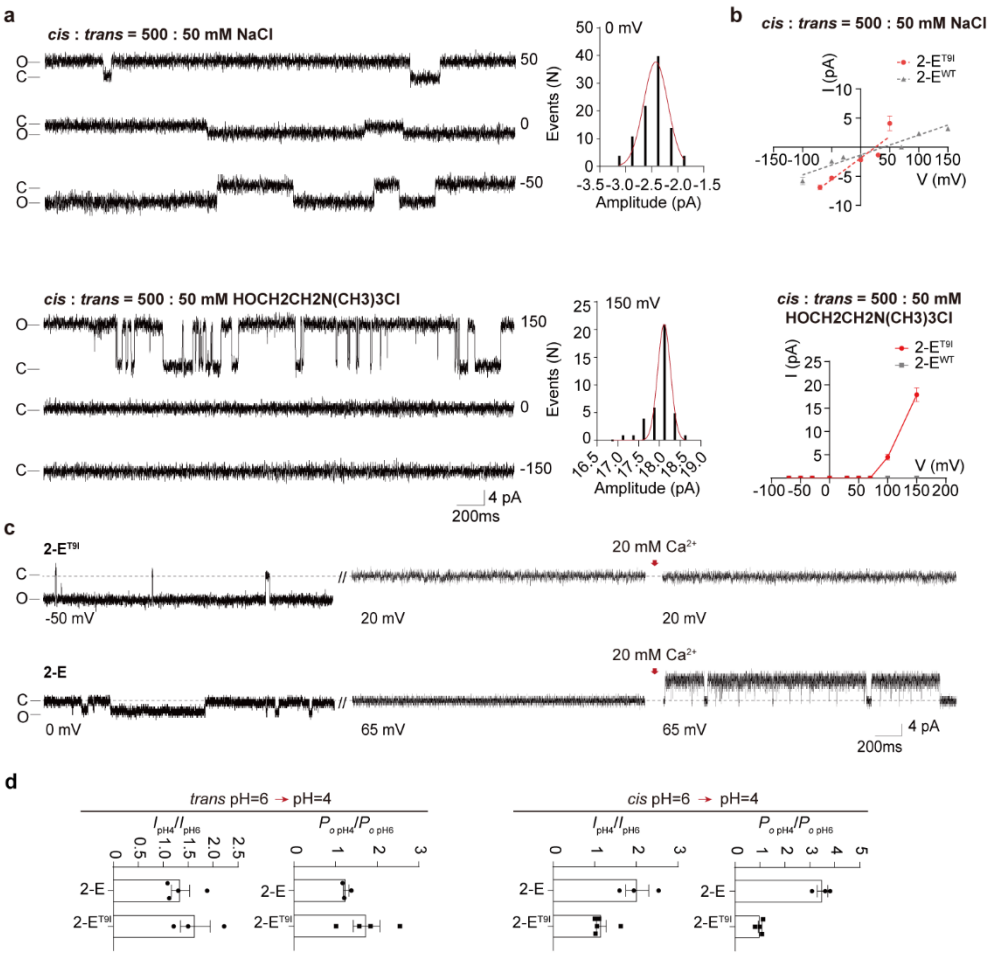

Supplementary information, Fig. S2 Electrophysiological property of T9I.

a. Single-channel current recording of T9I after reconstitution in lipid bilayers with PC/PS = 3:2 lipids at indicated potentials and solutions. Protein (5–50 ng/mL) was added to the cis side. All-point current histograms for the left trace (0, 150mV) ("C" means Closed; "O" means Open). **b.** *I-V* curves of T9I in indicated solutions (n ≥ 3). **c.** Pure Ca^{2+} currents recording in 50 :500 mM KCl solutions (*trans*: *cis*) via calcium titration as indicated concentrations, red arrow represents titration of $CaCl_2$. **d.** Amplitude (*I*) and open probability (P_o) of channel current at pH 4 were normalized to channel current at pH 6 of both sides (n ≥ 3).

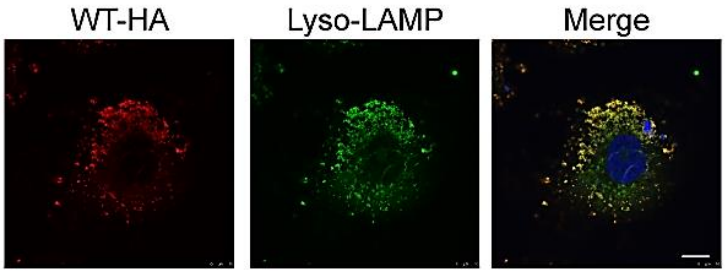

Supplementary information, Fig. S3 Wild type envelope protein (E) is co-localized with lysosome. Cell immunofluorescence of WT (Red) and lysosome marker (Green). Scale bar,10 μM.

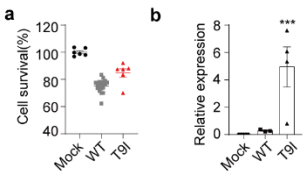

Supplementary information, Fig. S4 Cell viability of Vero E6 cells after transfection with 2-E plasmids and expression level of after transfection with WT

359 **andT9I.**

360 **a.** Cell viability of Vero E6 cells after transfection with WT, T9I or Vector (Mock) at

361 24 h. **b.** Expression level of 2-E after transfection with WT, T9I or Mock in Raw

362 264.7 cells detected by RT-qPCR.

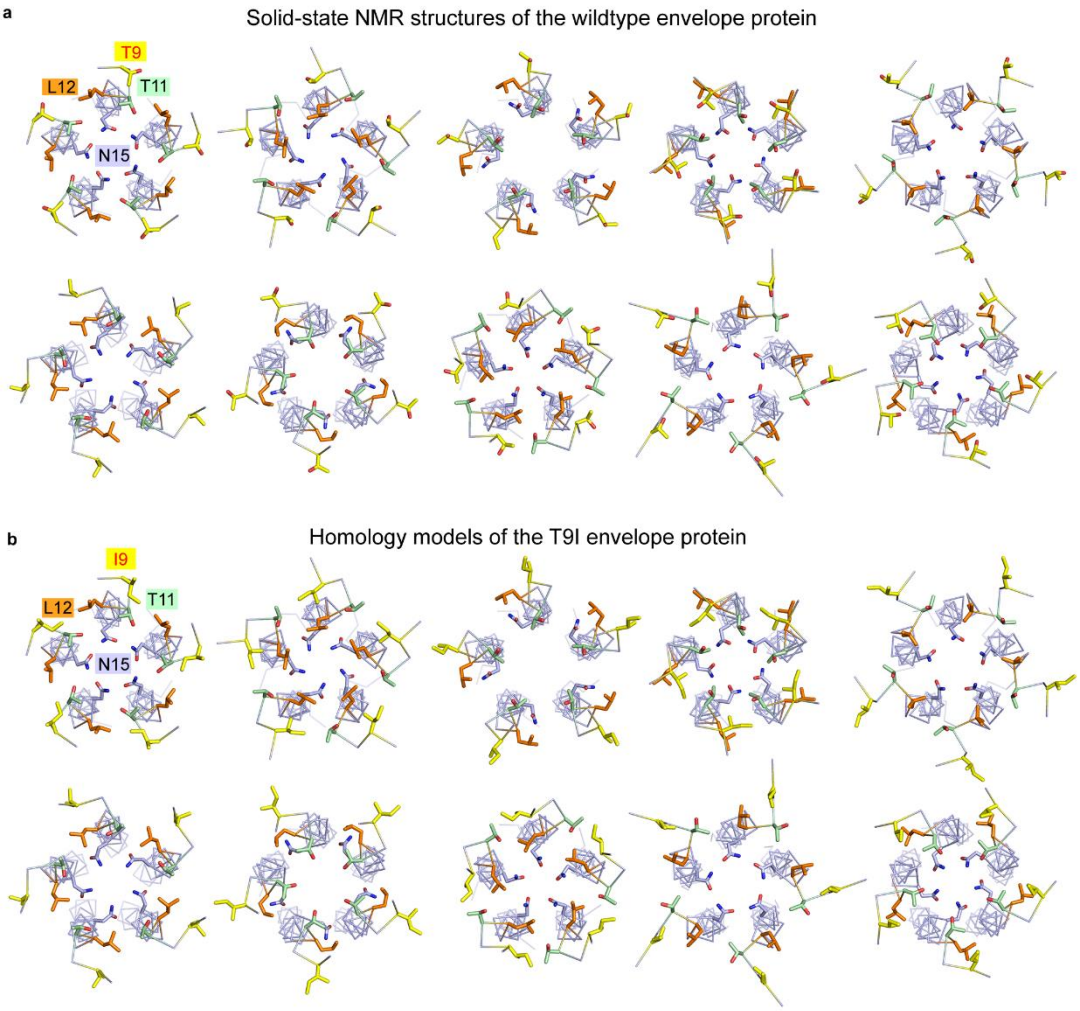

363

364 **Supplementary information, Fig. S5 Structure of WT and T9I.**

365 **a**, Top view of ten lowest-energy solid-state NMR structures of wildtype SARS-CoV-2

366 E protein (PDB code: 7k3g). Three N-terminal residues T9, T11, L12 and a pore-lining

367 residue N15 are shown as sticks (T9 in *yellow*, T11 in *green*, L12 in *orange*, N15 in

368 *light blue*). The protein is shown as ribbon. **b,** Top view of ten homology models of2-
369 E^{T9I}, which built based on the solid-state NMR structures of wildtype SARS-CoV-2
370 envelope protein (PDB code: 7k3g). Three N-terminal residues I9, T11, L12 and a pore-
371 lining residue N15 are shown as sticks (I9 in *yellow*, T11 in *green*, L12 in *orange*, N15
372 in *light blue*).